3D-reconstructions for the estimation of ice particle's volume using a two-views interferometric out-of-focus imaging set-up

Marc Brunel, Barbara Delestre, M. Talbi

Review of Scientific Instruments

3D-reconstructions for the estimation of ice particle's volume using a two-views interferometric out-of-focus imaging set-up

Cite as: Rev. Sci. Instrum. **90**, 053109 (2019); https://doi.org/10.1063/1.5085279
Submitted: 11 December 2018 . Accepted: 29 April 2019 . Published Online: 21 May 2019

M. Brunel, B. Delestre, and M. Talbi

Review of Scientific Instruments ARTICLE scitation.org/journal/rsi

3D-reconstructions for the estimation of ice particle's volume using a two-views interferometric out-of-focus imaging set-up

Cite as: Rev. Sci. Instrum. 90, 053109 (2019); doi: 10.1063/1.5085279
Submitted: 11 December 2018 • Accepted: 29 April 2019 •
Published Online: 21 May 2019

M. Brunel,[a] B. Delestre, and M. Talbi

AFFILIATIONS

UMR CNRS 6614 CORIA, Université de Rouen, Avenue de l'Université, Saint-Etienne du Rouvray 76801, France

[a]marc.brunel@coria.fr

ABSTRACT

The characterization of ice crystals has important applications in airborne research and civil aviation. Interferometric out-of-focus imaging is a promising technique. We investigate in this study the impact of the 3D shape reconstruction of the particles from a pair of interferometric images on the estimation of the ice particle's volume. An interferometric image gives indeed the 2D autocorrelation of the particle's shape. As different shapes can exhibit a similar 2D autocorrelation, particles of different shapes can have similar interferometric images. In this study, the volume of ice particles is estimated from a pair of interferometric images (with two perpendicular angles of view). The relative error in the particle's volume estimation is shown to be around $\Delta V/V \approx 30\%$ depending on the choice of the initial 3D particle's shape. It appears that the choice of the shape of the particle for both angles of view has a lower impact on the estimation of the particle's volume than the other sources of errors due to image acquisitions themselves.

I. INTRODUCTION

The characterization of irregular particles has important applications in meteorology, environment and safety, combustion, sprays, cosmetics, biology, and so on. Many theoretical, numerical, and experimental studies are carried out.[1] The realization of a system that can combine a 3D location of the particles in a flow, and a full characterization of each particle (size and 3D shape) would be of particular interest.[2–4] In many hostile environments, such a system should combine a large measurable particle size range, a high working distance between the medium under study and the instrument, and possibly an adjustable field of view to analyze simultaneously many particles.

An important application is the characterization of ice crystals in clouds, which is essential for meteorology, aircraft safety, and energy savings. Interferometric out-of-focus imaging of rough particles offers a very promising solution.[4] Initially developed to analyze spherical droplets or bubbles,[5–16] it can be extended to rough particle sizing through the processing of speckle-like patterns.[17–24] The field of view can reach tens of cm^2, the working distance can exceed 10 cm, and the technique is scalable in such a way that the size range can cover 2 decades: from tens of micrometers to a few millimeters. In recent years, configurations enabling a 3D location of particles with a sole CCD sensor, or multiviews acquisition systems that can perform a 3D shape recognition of particles have been demonstrated.[25,26]

A difficulty is due to the nature of the signal delivered by the speckle-like out-of-focus image of the particles. Under simplifying assumptions, the 2D Fourier transform of the interferometric image is shown to give the 2D autocorrelation of the contour of the bright part of the particle.[24] This result has been validated in many experimental situations, with different kinds of rough particles as ice crystals.[25–31] Unfortunately, the knowledge of the contour of the 2D autocorrelation of a 2D object does not give the knowledge of the contour of the 2D object itself. Different 2D objects can indeed exhibit similar 2D autocorrelations. When performing a double-view setup in order to estimate the volume of ice particles, an assumption about the 3D shape of the particle is thus done: particles were likened to ellipsoidal objects in Ref. 26. As the accuracy of ice water content estimation is crucial for airborne applications, it is necessary to understand the level of error that can be generated by this source of error. This is the aim of the present study.

In order to do this, the volumes of different reconstructed 3D particles whose 2D projections exhibit similar 2D autocorrelations will be compared. Each particle will be observed from two perpendicular angles of view to enable an approximate 3D reconstruction. The volume of the different possible reconstructed particles will then be compared to the volume of the real particle estimated from the pair of in-focus images recorded simultaneously. The article will detail the different steps of the analysis: the first step has been to realize interferometric imaging of ice particles, generated in a freezing column,[32] from two perpendicular angles of view.[26] These experiments are synchronized with in-focus imaging of the same particles using two other CCD sensors. The second step is to perform image processing of the recorded interferometric patterns, i.e., 2D Fourier transforms that are then likened to the 2D autocorrelations of the projections of the initial particle on a plane, according to the experimental angles of view. The next step is then to realize 2D reconstructions of possible 2D contours whose 2D autocorrelations match the experimental results. Finally, different possible 3D objects are reconstructed. Their interferometric imaging "signatures" are compatible with the experimental results obtained from the two angles of view. Their volume is estimated and compared to the estimation obtained from the real in-focus images of the same ice particle. The article describes this procedure and shows results obtained in two cases: when the 2D Fourier transforms of the interferometric patterns deliver convex shapes or shapes with pronounced concavity.

II. ANALYSIS OF CONVEX SHAPES

A. Experimental setup

The experimental setup is presented in Fig. 1. It has been described in Ref. 26. Liquid droplets are injected in a cold chamber,[32] fall and freeze. Optical windows are at the bottom of the column to ensure laser illumination and image acquisition. Ice particles are illuminated by 4 ns, 5 mJ, 532 nm pulses emitted by a frequency doubled Nd:YAG laser. Two out-of-focus imaging lines enable interferometric imaging of particles from two perpendicular angles of view. In the configuration that we use, optical collection through the windows is ensured in backward directions that correspond to scattering angles of +135° and −135°. Two beam splitters are used to record simultaneously the in-focus images (sensors 1 and 3) associated with the corresponding out-of-focus images of the same particle (sensors 2 and 4). The view observed with sensors 1 and 2 will be called view 1. The view observed with sensors 3 and 4 will be called view 2. In-focus images are obtained using far-field ISCOOPTIC objectives (fields of view 2.45 mm × 2.45 mm, depth of field 1 mm). Out-of-focus systems consist of Nikon objectives (focus length of 180 mm). The CCD sensors used for in-focus imaging are composed of 2048 × 2048 pixels (pixel size: 5.5 μm). The CCD sensors used for the out-of-focus imaging are composed of 1920 × 1200 pixels (pixel size: 5.86 μm). The four CCD sensors are synchronized on the laser pulse for synchronized acquisitions. The reference frame (x, y, z) is presented in Fig. 1 for clarity. After 2D Fourier transforms of the interferometric images, the corresponding coordinates in spectral domain will be noted (u, v, w). Extension tubes provide out-of-focus imaging. In-focus images are used to validate the analyses deduced from out-of-focus images. Nevertheless, the low field of view of in-focus systems makes the recording of images long: we are actually "waiting" for particles in the field of view of the in-focus imaging lines. An on-board instrument would just be composed of the out-of-focus imaging lines.

B. Tri-intersection method

In a simplified approximation, the electric field scattered by a rough particle under laser illumination is assumed to be given

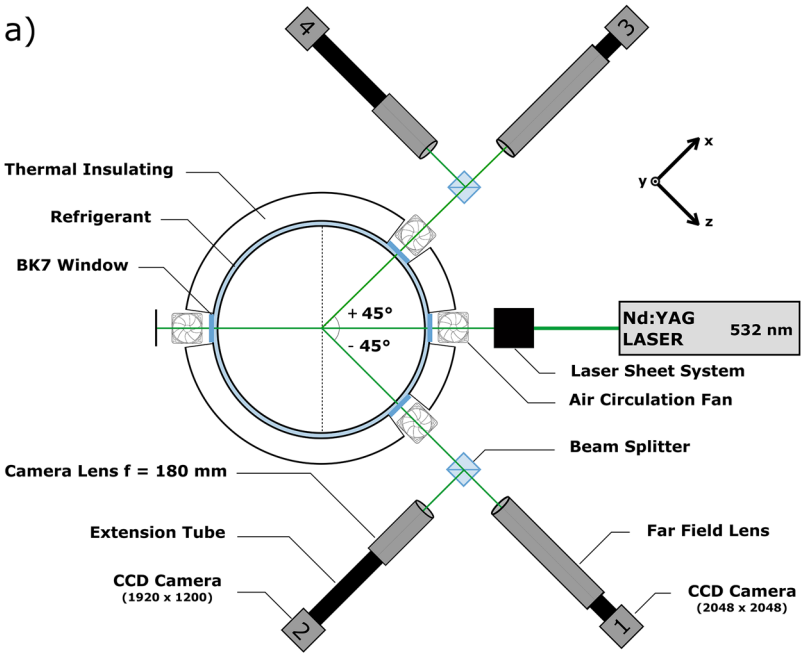

FIG. 1. Experimental setup.

by $G_0(x_0, y_0) = \sum_{j=1}^{N_{gp}} \alpha_j e^{i\varphi_j} \delta_{2D}(x_0 - a_j, y_0 - b_j)$, where the δ_{2D} functions are Dirac functions, N_{gp} is the number of point light sources located on the particle, a_j and b_j are the transverse coordinates of glare point denoted j, and α_j is the amplitude of glare point j and φ_j its phase. Neglecting the role of the aperture of the imaging system (large aperture), the electric field G(x, y, z) can be calculated in the plane of the CCD sensor using a generalized Huygens-Fresnel integral.[20,21] It is given vs coefficients A_{tot}, B_{tot}, C_{tot}, and D_{tot} of the optical transfer matrix between the plane of the different emitters and the plane where the CCD sensor is located. The 2D Fourier transform of the intensity in the plane of the CCD sensor $FT_{2D}[I](\lambda B_{tot}u, \lambda B_{tot}v)$ and the 2D autocorrelation of the initial repartition of the point emitters $A_{2D}[G_0](dx, dy)$ are not rigorously equal.[24] Nevertheless, assuming that all pairs ($a_j - a_k$, $b_j - b_k$) are unique (which is easily satisfied in the case of perfect point emitters), we obtain[24]

$$|FT_{2D}[I](\lambda B_{tot}u, \lambda B_{tot}v)| \propto |A_{2D}[G_0](dx, dy)|. \quad (1)$$

Based on this relation, the numerical values of both functions can be compared in any point $(\lambda B_{tot}u, \lambda B_{tot}v)$ and (dx, dy), respectively. In practice, our attention has been limited to the comparison of the contours of both functions in previous studies: after recording of an interferometric out-of-focus image, its 2D Fourier transform is binarized and the contour can be likened to the contour of the 2D autocorrelation of the particle itself. This procedure has been validated experimentally in many cases encountered.[24–31] This property offers very interesting applications in particle sizing or shape recognition. Unfortunately, the 2D autocorrelation of an object does not give the object itself. But methods exist to predict possible objects whose 2D autocorrelation match an expected one.[33–35]

Let us briefly recall the tri-intersection method that can be used to do this.[33] We consider a convex centrosymmetric 2D object called A (see Fig. 2). We define a first vector $\boldsymbol{\omega}_1$ whose origin is the center of A and whose vector's extremity is on the border of A, noted ∂(A). The copy of the initial object A, translated from $\boldsymbol{\omega}_1$, is called $(A + \omega_1)$. We define then a second vector $\boldsymbol{\omega}_2$, whose origin is the center of A and whose vector's extremity is at the intersection of the borders of A and $(A + \omega_1)$. The copy of the initial object A translated from $\boldsymbol{\omega}_2$ is called $(A + \omega_2)$. Finally, the object B defined by the tri-intersection $B = A \cap (A + \omega_1) \cap (A + \omega_2)$ has a 2D autocorrelation that matches the initial object A. This property is valid whatever the choice of the initial vector $\boldsymbol{\omega}_1$, provided that the vector's origin is the center of A and the vector's extremity is on the border ∂(A) of A. Based on this method, we have developed a program that delivers six possible 2D shapes of a 2D object whose 2D autocorrelation is deduced from the 2D Fourier transform of any interferometric pattern recorded experimentally. The choice of six shapes, from six initial vectors $\boldsymbol{\omega}_1$, is arbitrary and could be modified. We have actually determined more than 6 shapes per interferometric image when performing our study. The number of shapes has been limited to 6 here in order to present visible figures (Figs. 5–7, 14–16) and also in order to estimate a significant number of particle's volumes combining two angles of view: $6 \times 6 = 36$. The shapes that will be presented in the next figures correspond to panels that cover, as well as possible the variety of shapes that could be obtained with our different experimental results. With our program, we could predict automatically $\ll n \gg$ possible shapes with a choice of $\ll n \gg$ vectors $\boldsymbol{\omega}_1$, oriented according to the angle ($k\pi/n$) in relation to the horizontal axis ($k \in [\![0, n-1]\!]$). In practice, the choice of the initial vector $\boldsymbol{\omega}_1$ governs strongly the final shape that will be obtained. The principle of an automated program to determine n possible shapes can be summarized as follows:

- 2D Fourier transform of the interferometric image.
- Contour detection: obtention of the contour of object A.
- For k = 0 to n–1:
  - Determination of the extremity of vector $\boldsymbol{\omega}_1$, oriented according to the angle ($k\pi/n$) in relation to the horizontal axis.
  - First translation of the contour of object A to determine the contour of object $(A + \omega_1)$.
  - Determination of the extremity of vector $\boldsymbol{\omega}_2$ (intersection point).
  - Second translation of the contour of object A to determine the contour of object $(A + \omega_2)$.
  - Filling and binarization of the three contours of objects A, $(A + \omega_1)$, and $(A + \omega_2)$.
  - Calculus of the product: $A \times (A + \omega_1) \times (A + \omega_2)$. Determination of the possible shape B_k.

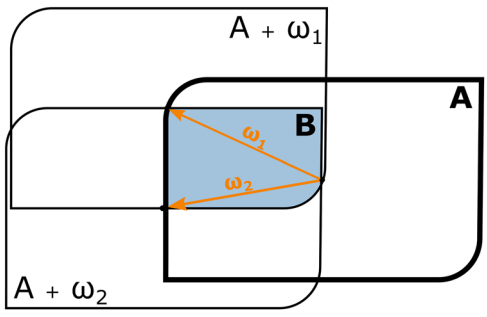

FIG. 2. Principle of the tri-intersection method.

C. First case: Analysis of convex shapes

In the first case that will be presented, the 2D autocorrelations obtained have quite perfect convex shapes. The tri-intersection method is thus particularly well adapted. Figure 3(a) shows the 2D Fourier transform of the interferometric out-of-focus images (not reported) of a first ice particle. It corresponds to view 1: observation of the (xy) plane. Its contour is then filled and binarized as presented in Fig. 3(b). This step is necessary as the analysis is based on the correspondence between the contour of the binarized 2D Fourier transform of the interferometric image and the 2D autocorrelation of the particle's shape [relation (1)]. We have no possibility to estimate the error that it induces: (i) theoretically, a deeper comparison between both functions would require the development of exact light scattering simulations that are not available to describe irregular rough particles of any shape and texture; (ii) experimentally, we have not the possibility to generate in the freezing column calibrated ice particles of perfectly known 3D shape (the simultaneous observation of the in-focus images of the particles from the

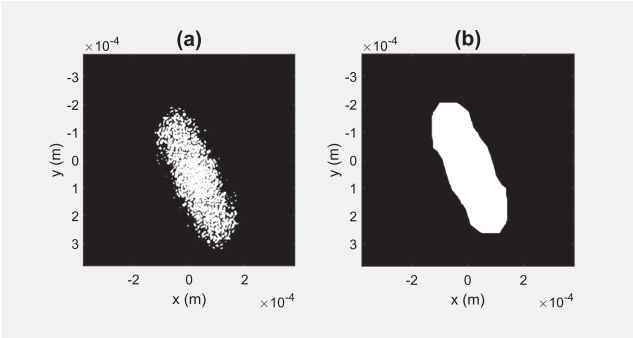

FIG. 3. 2D Fourier transform of the interferometric out-of-focus image of an ice particle from view 1 (xy plane) (a) and its filled and binarized contour (b).

same angles of view is the best solution that we found, using sensors 1 and 3). The first out-of-focus image has been recorded with sensor 2. Figure 4(a) shows then the 2D Fourier transform of the interferometric out-of-focus image (not reported) of the same ice particle recorded with sensor 4. Image acquisitions have been done simultaneously with sensors 2 and 4. Figure 4(b) shows the filled and binarized contour. Based on relation (1), these 2D Fourier transforms are likened to the 2D autocorrelations of the particle's shape, for both angles of view respectively. Let us now proceed to the reconstruction of possible objects. The tri-intersection method is used to predict possible 2D shapes that would have similar 2D autocorrelations. The 2D -autocorrelations that will be considered and used in what follows are those presented in Fig. 3(b) for view 1 and Fig. 4(b) for view 2.

The tri-intersection method is thus applied to reconstruct possible objects respecting the experimental results observed on both views. Figures 5(a)–5(f) show 6 possible 2D objects whose 2D autocorrelations correspond to the one of Fig. 3(b), i.e., to view 1. The x-axis and y-axis units are in meters. They show the exact dimensions of the possible particles after application of the scaling coefficient (λB_{tot}). For comparison with the initial function, we can calculate the 2D autocorrelations of these six possible objects.

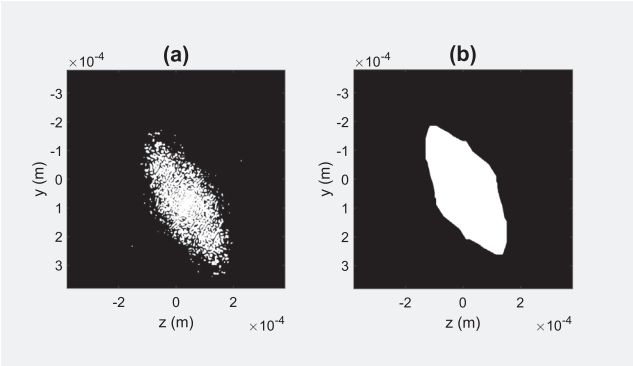

FIG. 4. 2D Fourier transform of the interferometric out-of-focus image of an ice particle from view 2 (zy plane) (a) and its filled and binarized contour (b).

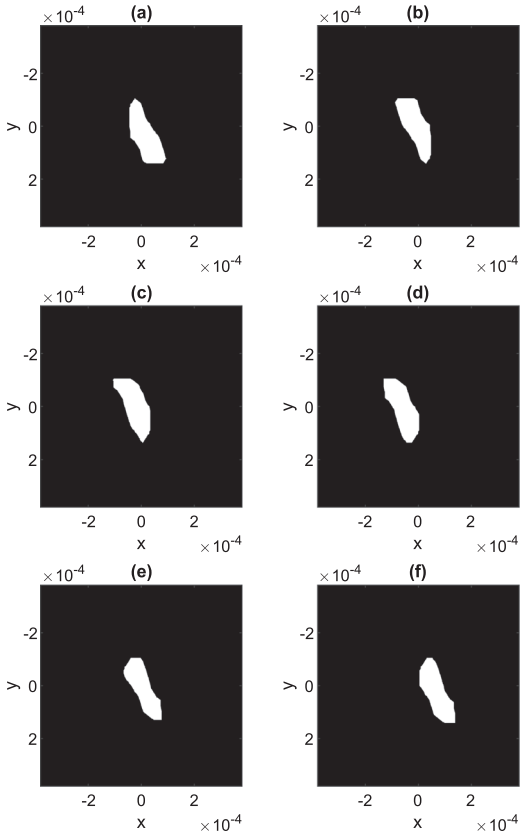

FIG. 5. Six possible shapes [(a)–(f) respectively] whose 2D autocorrelation gives the one of Fig. 3(b) [from view 1, (xy) plane].

Figures 6(a)–6(f) show then the difference between the initial binarized 2D Fourier transform of the interferometric pattern [observed on view 1, Fig. 3(b)] with the calculated 2D autocorrelation of the predicted object (for all 6 objects respectively). The gray color indicates that there is no difference between both functions. The white color indicates zones where the 2D Fourier transform is larger. The black color indicates zones where the 2D autocorrelation is larger. We can see that the differences remain very limited. The shape predictions using the tri-intersection method are satisfactory.

Using the tri-intersection method again, Figs. 7(a)–7(f) show now 6 possible 2D objects whose 2D autocorrelations correspond to the one of Fig. 4(b), i.e., to view 2. As in previous case, we could report the differences between the initial binarized 2D Fourier transform of the initial pattern and the 2D autocorrelations of the predicted shapes. We would show that predictions are in good agreement with the experimental pattern. These different shapes obtained for views 1 and 2 are then combined to reconstruct different 3D objects that respect the experimental results on both views. The principle of this reconstruction can be explained as follows: we realize a mask corresponding to one possible object for view 1 and a mask corresponding to one possible object for view 2. The 3D object reconstructed is the one that would be obtained from a

photopolymerization process obtained from a first UV-laser incident on mask 1 while a second UV laser would be incident on mask 2 on a perpendicular axis, as illustrated in Fig. 8. It is thus assumed that there is no hole in the reconstructed object. After this reconstruction process, the volume of the reconstructed 3D object is evaluated. As 36 combinations can be done (6 for view 1 × 6 for view 2), we obtain 36 possible values for the volume of the ice particle. These 36 volume's estimations are reported in Fig. 9.

The experimental setup enables the simultaneous recording of interferometric out-of-focus images (sensors 2 and 4 in Fig. 1) and in-focus images under the same angle of view (sensors 1 and 3 in Fig. 1). It is thus possible to estimate the volume of the same particle from a pair of in-focus images. Figure 10(a) shows the binarized in-focus image of the particle observed from view 1 (sensor 1). Binarization allows us to enhance the contrast of the different "glare"points located on this irregular rough particle under laser illumination. The contour of these different bright spots is then filled. The resulting contour is presented in Fig. 10(b). In a similar way, Fig. 11(a) shows the binarized in-focus image of the particle observed from view 2 (sensor 3). As previously, the contour of the different bright spots is then filled leading to the 2D shape of Fig. 11(b). The 3D shape of the particle is then reconstructed in a very similar way as previous 3D reconstructions. According to the projection method illustrated in Fig. 8, the mask 1 in the xy-plane is the contour of Fig. 10(b), while mask 2 in the zy-plane is the contour of Fig. 11(b). It is assumed again that there is no hole in the reconstructed object. After this reconstruction process, the volume of the reconstructed 3D object is evaluated. It is plotted as an horizontal plain red line in Fig. 9.

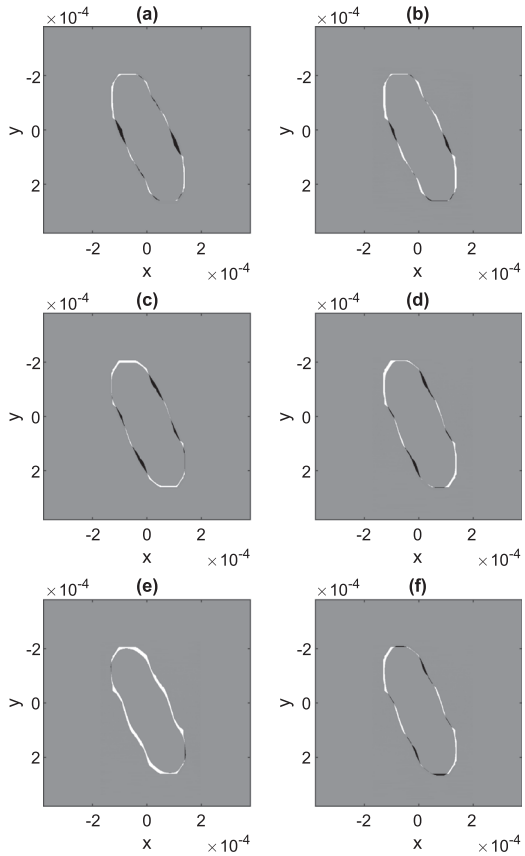

FIG. 6. Subtractions of the 2D autocorrelations of the shape of Fig. 5(p) [in subfigure (p)] with the shape of Fig. 3(b) deduced from experiment [with (p) = (a)–(f) respectively]. Black: the original one is higher; white: the reconstructed one is higher; gray: no difference.

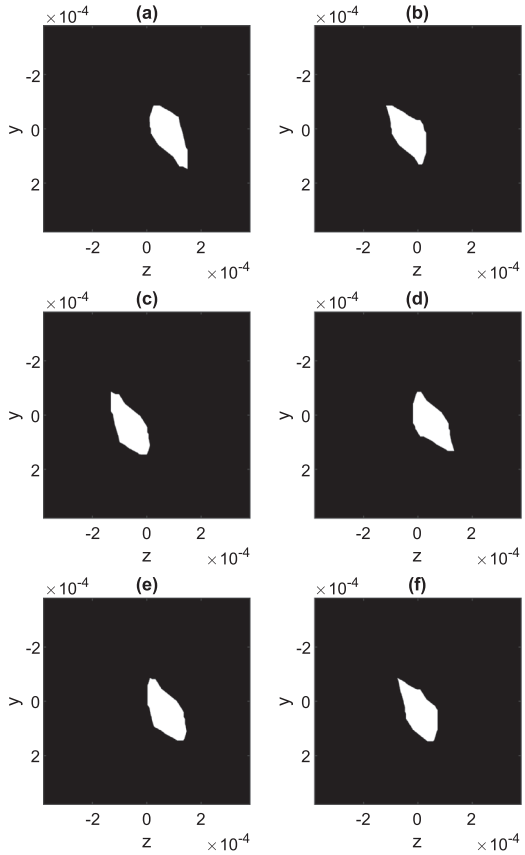

FIG. 7. Six possible shapes [(a)–(f), respectively] whose 2D autocorrelation gives the one of Fig. 4(b) [view 2, (zy) plane].

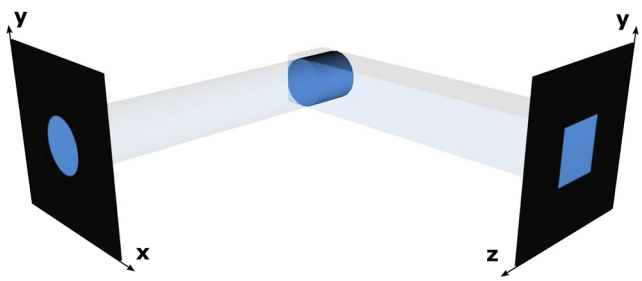

FIG. 8. Principle of the reconstruction of a 3D object from two projections.

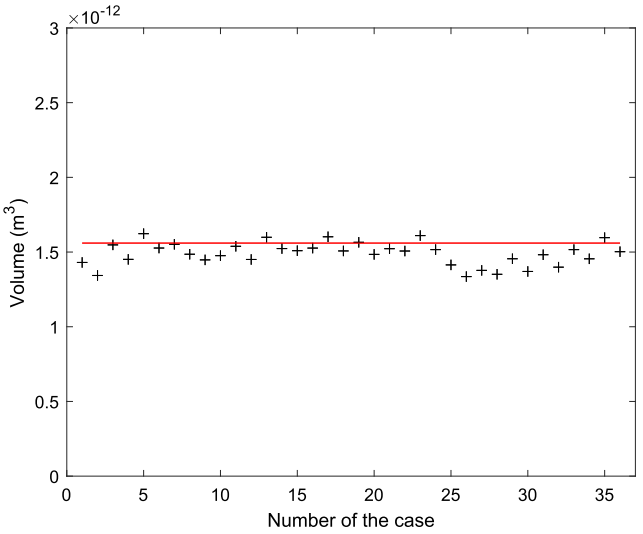

FIG. 9. Volumes of the 36 possible reconstructed particles (crosses) and value deduced from in-focus images (red).

These different results deserve discussion concerning the accuracy of the different estimations of particle's volumes. For the out-of-focus images, there are two sources of errors when measuring the size of the particle. The first one is the estimation of parameter λB_{tot} that is necessary for axis-scaling after 2D Fourier transform (see Sec. II B): it corresponds actually to a proper estimation of the defocus parameter. The second source of error is the definition of the binarization threshold after 2D Fourier transform. For example, the size of this particle along axis y is estimated to be $y_p \pm \Delta y_p = 235 \pm 20\ \mu$m. The particle's volume would then be deduced with an accuracy estimated to be around $\Delta V/V = \Delta x_p/x_p + \Delta y_p/y_p + \Delta z_p/\Delta z_p \approx 30\%$. Uncertainty is actually higher because the 3D reconstruction introduces its own sources of error: no knowledge of the xz view of the particle and thus assumption of a convex shape on this view; assumption that there is no hole inside the particle. These errors are very difficult, even impossible to estimate. For size estimations using in-focus images, the main source of error is the binarization process of the image, followed by the filling process of the contour, which tends in general to enlarge

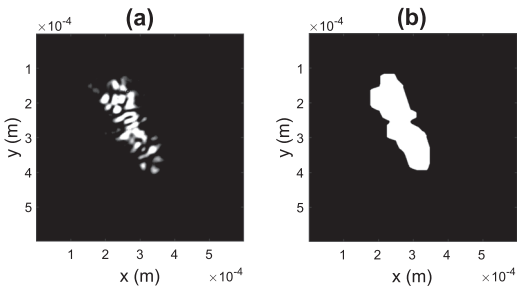

FIG. 10. In-focus image of particle 1 (a), and its filled and binarized contour (b) [view 1, (xy) plane].

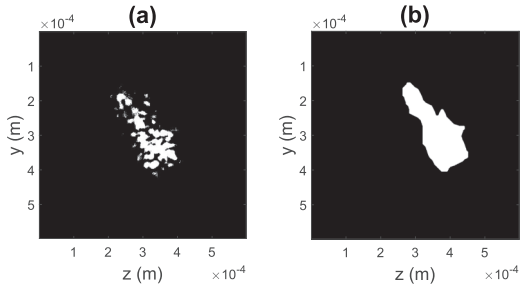

FIG. 11. In-focus image of particle 1 (a), and its filled and binarized contour (b) [view 2, (zy) plane].

the particle. Another source of error is the magnification factor of the in-focus imaging line. It is known with better precision using an initial calibration. It equals $|\gamma| = 4.65$. The size of the particle along axis y is estimated to be $y_p \pm \Delta y_p = 265 \pm 20\ \mu$m using in-focus imaging. The estimation of the particle's volume relative error would then be around $\Delta V/V = \Delta x_p/x_p + \Delta y_p/y_p + \Delta z_p/\Delta z_p \approx 30\%$. But uncertainty is actually higher because, as previously, the 3D reconstruction introduces its own sources of error. Nevertheless, what we want to illustrate with this Fig. 9 is that the choice of the shapes of the particle for both angles of view using the tri-intersection method has actually a lower impact on the estimation of the particle's volume than the other sources of errors due to image acquisitions themselves (with the knowledge of the experimental parameters). The dispersion of the particle's volume estimations in Fig. 9 remains indeed relatively small. This result is actually quite remarkable.

III. ANALYSIS OF SHAPES WITH PRONOUNCED CONCAVITY

The tri-intersection method is well adapted to cases where the initial shape corresponding to the 2D autocorrelation of an object is convex. It was nearly the case in Sec. II C: see the contours of Figs. 3(b) and 4(b) for views 1 and 2. In practice, this case should not be the most frequent. It is thus important to know whether

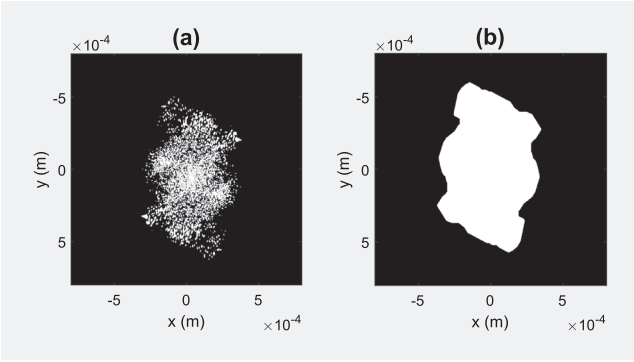

FIG. 12. 2D Fourier transform of the interferometric out-of-focus image of an ice particle from view 1 (xy plane) (a) and its filled and binarized contour (b).

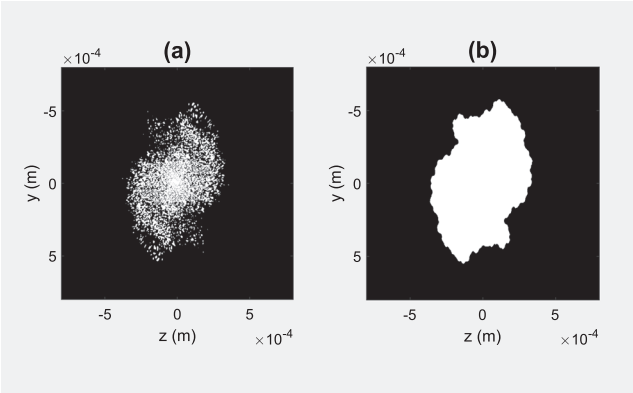

FIG. 13. 2D Fourier transform of the interferometric out-of-focus image of an ice particle from view 2 (zy plane) (a) and its filled and binarized contour (b).

similar volume estimations can be done although the initial experimental results deliver shapes with pronounced concave parts, and whether these estimations are still comparable with the real volumes of the particles. We present thus in this new section a second example. The organization of the results will be quite similar. It will show that although the volume estimation is less accurate, it is still acceptable. Figure 12(a) shows the 2D Fourier transform of the interferometric out-of-focus image (not reported) of an ice particle from view 1 [plane (xy)]. The contour deduced from 2D Fourier transform of the interferometric patterns is first filled and then binarized, as shown in Fig. 12(b). In a similar way, Fig. 13(a) shows the 2D Fourier transform of the interferometric out-of-focus image of the same ice particle from view 2 [plane (zy)], and Fig. 13(b) shows its filled and binarized contour. We can note that for both views, the contours are clearly not convex.

Figures 14(a)–14(f) show then 6 possible 2D objects whose 2D autocorrelations match the one of Fig. 12(b), i.e., correspond to view 1. Figures 15(a)–15(f) show the difference between the initial binarized 2D Fourier transform of the interferometric pattern [observed on view 1, Fig. 12(b)] with the calculated 2D autocorrelation of the predicted object (for all 6 objects, respectively). The differences appear larger, specifically in the domains where concavity is the most pronounced. Nevertheless, error remains limited. The shape predictions using the tri-intersection method are not so good but remain satisfactory. We consider then view 2 of the same

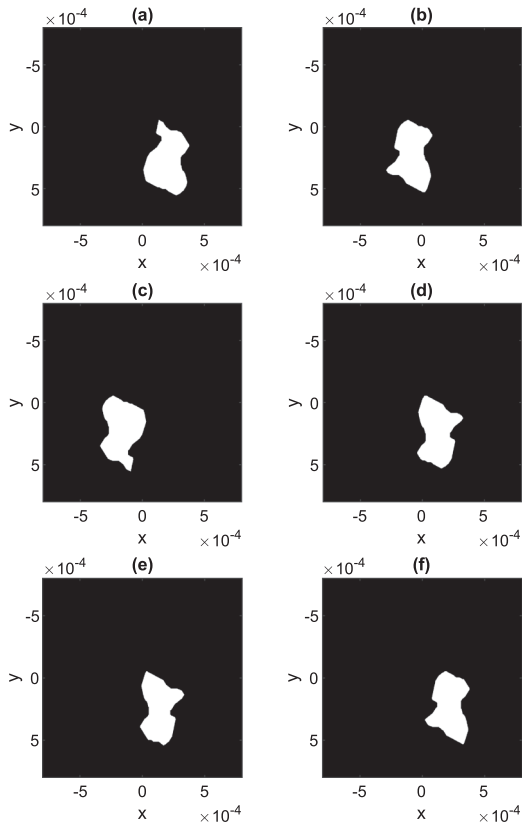

FIG. 14. Six possible shapes [(a)–(f), respectively] whose 2D autocorrelation gives the one of Fig. 12(b) [view 1, (xy) plane].

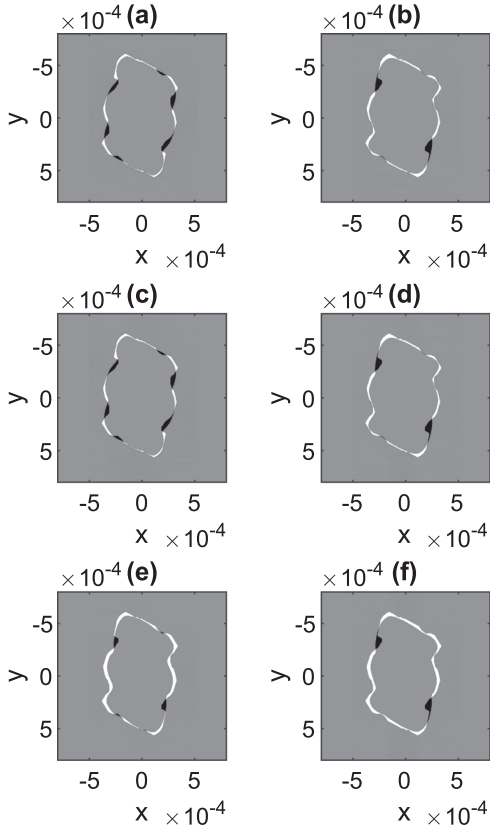

FIG. 15. Subtractions of the 2D autocorrelations of the shape of Fig. 14(p) [in subfigure (p)] with the shape of Fig. 12(b) deduced from experiment [with (p) = (a)–(f) respectively]. Black: the original one is higher; white: the reconstructed one is higher; gray: no difference.

particle. Figures 16(a)–16(f) show 6 possible 2D objects whose 2D autocorrelations match the one of Fig. 13(b). We do not present the subtractions of the 6 reconstructed 2D autocorrelations with the original one as done in Fig. 15 for view 1. But conclusions would be very similar for this second view.

These different shapes obtained for views 1 and 2 are then combined to reconstruct different 3D objects that respect the experimental results on both views. A first mask corresponding to one possible object for view 1 and a second mask corresponding to one possible object for view 2 are considered to realize the 3D object reconstruction as illustrated in Fig. 8. The volume of the reconstructed 3D object is then evaluated. As 36 combinations can be done (6 for view 1 × 6 for view 2), 36 possible values for the volume of the ice particle are obtained. These 36 volume's estimations are reported in Fig. 17.

As in Sec. II C, the volume of the same particle is now estimated from the pair of in-focus images recorded simultaneously. Figure 18(a) shows the in-focus image of the particle observed from view 1 (sensor 1). The contour is then filled, giving Fig. 18(b). Figure 19(a) shows the in-focus image of the particle observed from view 2 (sensor 3), and Fig. 19(b) the filled contour. The 3D shape of the particle is then reconstructed through projections as illustrated in Fig. 8. The mask 1 in the xy-plane is the contour of Fig. 18(b),

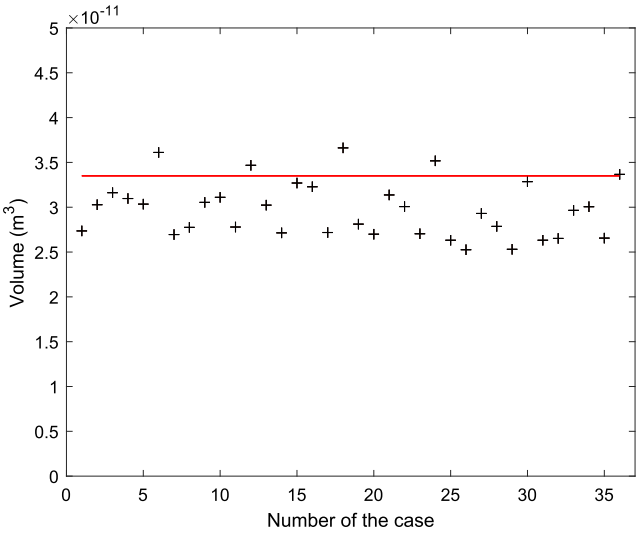

FIG. 17. Volumes of the 36 possible reconstructed particles (crosses) and value deduced from in-focus images (red).

while mask 2 in the zy-plane is the contour of Fig. 19(b). The volume of this reconstructed 3D object is then evaluated. It is plotted as an horizontal plain red line in Fig. 17. It is in the range of estimations made using the reconstructions issued from the analysis of out-of-focus images. For the out-of-focus images, the sources of errors are still a proper estimation of the defocus parameter and the definition of the binarization threshold after 2D Fourier transform. As the particle is larger, the error is slightly smaller because the intensity of the signal received by the CCD sensor is higher. The particle's volume is then deduced with an accuracy estimated to be around $\Delta V/V \approx 25\%$. As in previous case, uncertainty concerning the 3D reconstruction is difficult to estimate, essentially because there is no experimental knowledge of the xz view of the particle. For size estimations using in-focus images, the main source of error is the binarization process of the image, followed by the filling process of the contour. Due to these effects, the relative error on the particle's volume is around $\Delta V/V = 25\%$. Uncertainty is actually higher because, as previously, the 3D reconstruction introduces its own sources of error. We can observe in Fig. 17 that the

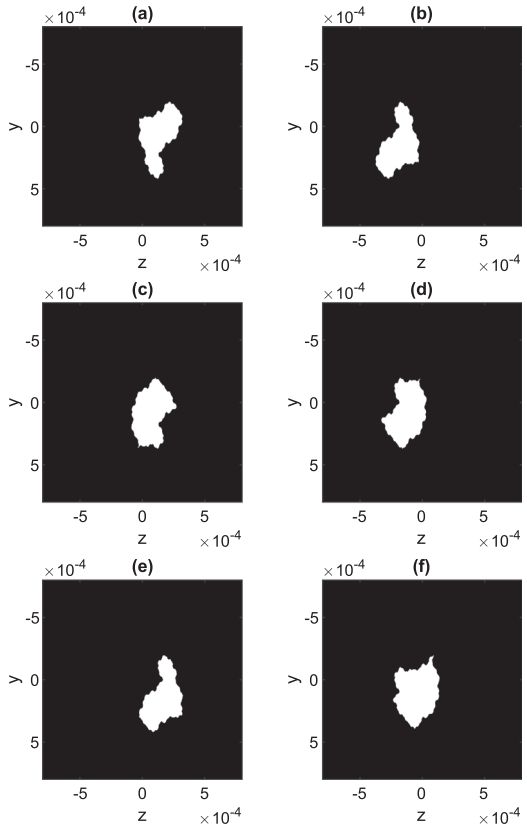

FIG. 16. Six possible shapes [(a)–(f), respectively] whose 2D autocorrelation gives the one of Fig. 13(b) [view 2, (zy) plane].

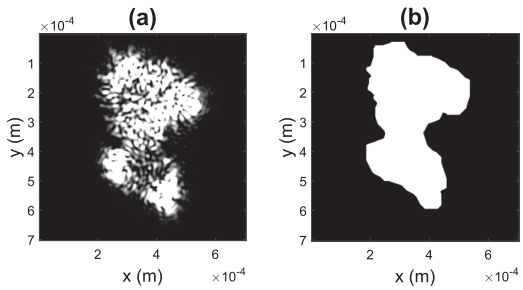

FIG. 18. In-focus image of particle 2 (a), and its filled and binarized contour (b) [view 1, (xy) plane].

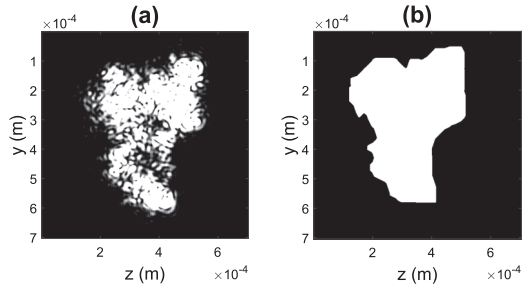

FIG. 19. In-focus image of particle 2 (a), and its filled and binarized contour (b) [view 2, (zy) plane].

dispersion of the 36 volume's estimations is higher than in Sec. II C. Nevertheless, although the experimental shapes of Figs. 12(b) and 13(b) present significant concavities, the choice of the shapes of the particle for both angles of view using the tri-intersection method has a reduced impact, just comparable to the other sources of errors due to image acquisitions themselves.

IV. CONCLUSION AND PERSPECTIVES

Recent studies showed that the 2D Fourier transform of the interferometric image of an ice particle can be likened to the 2D autocorrelation of the contour of the bright part of the particle. This result has been validated in many experimental situations. Unfortunately, the knowledge of the contour of the 2D autocorrelation of a 2D object does not give the knowledge of the contour of the 2D object itself. Different 2D objects can indeed exhibit similar 2D autocorrelations. When performing a double-view setup in order to estimate the volume of ice particles, an assumption about the 3D shape of the particle is thus done: particles are likened to ellipsoidal objects for example.[26] As the accuracy of ice water content estimation is crucial for airborne applications, it is necessary to understand the level of error that can be generated by this problem using a tri-intersection to predict possible 3D objects that match experimental light scattering images. In this study, we have estimated the level of error due to the choice of the shape of the particle. We have seen that it remains relatively reasonable in comparison with other experimental sources of noise.

Based on relation (1), the numerical values of both functions $|FT_{2D}[I](\lambda B_{tot}u, \lambda B_{tot}v)|$ and $|A_{2D}[G_0](dx, dy)|$ could be compared in any point $\lambda B_{tot}u, \lambda B_{tot}v$ and (dx, dy), respectively. In our last experimental studies, the use of this relation has been limited to the comparison of the contours of both binarized functions.[24–31] If the relation between both functions could be validated experimentally in any point, a recent study shows that the uncertainty concerning the choice of the shape of the particle could be much reduced.[36] Experimental demonstrations are thus to be done in this direction. Relation (1) between both functions is clearly observed assuming that a scattering particle can be represented by a large number of point emitters randomly located on the envelope of the particle.[26] Exact light scattering simulations should be of particular interest in the future for enhanced exact shape recognition.[1,37–39]

ACKNOWLEDGMENTS

The authors thank the French National Agency for financial support through the "SIAMA" project of program Investissements d'Avenir LabEx EMC3 (Grant No. ANR-10-LABX-09-01), ANR ASTRID "NUAGE" (Grant No. ANR-15-ASTR-0003-01), Région Normandy for CPER and European Union for FEDER project "THESIS."

REFERENCES

[1] M. I. Mishchenko, J. M. Dlugach, M. A. Yurkin, L. Bi, B. Cairns, L. Liu, R. Lee Panetta, L. D. Travis, P. Yang, and N. T. Zakharova, Phys. Rep. **632**, 1–75 (2016).
[2] M. J. Berg and G. Videen, J. Quant. Spectrosc. Radiat. Transfer **112**, 1776–1783 (2011).
[3] Z. Ulanowski, P. H. Kaye, E. Hirst, R. S. Greenaway, R. J. Cotton, E. Hesse, and C. T. Collier, Atmos. Chem. Phys. **14**, 1649–1662 (2014).
[4] E. Porcheron, P. Lemaitre, J. van Beeck, R. Vetrano, M. Brunel, G. Gréhan, and L. Guiraud, J. Eur. Opt. Soc.: Rapid Publ. **10**, 15030 (2015).
[5] G. König, K. Anders, and A. Frohn, J. Aerosol Sci. **17**, 157–167 (1986).
[6] R. Ragucci, A. Cavaliere, and P. Massoli, Part. Part. Syst. Charact. **7**, 221–225 (1990).
[7] A. R. Glover, S. M. Skippon, and R. D. Boyle, Appl. Opt. **34**, 8409–8421 (1995).
[8] T. Kawaguchi, Y. Akasaka, and M. Maeda, Meas. Sci. Technol. **13**, 308–316 (2002).
[9] M. Maeda, T. Kawaguchi, and K. Hishida, Meas. Sci. Technol. **11**, L13–L18 (2000).
[10] N. Damaschke, H. Nobach, and C. Tropea, Exp. Fluids **32**, 143–152 (2002).
[11] S. Dehaeck and J. P. A. P. Van Beeck, Exp. Fluids **42**, 767–781 (2007).
[12] Y. Hardalupas, S. Sahu, A. M. K. P. Taylor, and K. Zarogoulidis, Exp. Fluids **49**, 417–434 (2010).
[13] H. Shen, S. Coetmellec, G. Grehan, and M. Brunel, Appl. Opt. **51**, 5357–5368 (2012).
[14] H. Shen, S. Coëtmellec, and M. Brunel, Opt. Lett. **37**, 3945–3947 (2012).
[15] R. S. Volkov, G. V. Kuznetsov, and P. A. Strizhak, Int. J. Heat Mass Transfer **96**, 20–28 (2016).
[16] H. Zhang, Y. Zhou, J. Liu, D. Jia, and T. Liu, Rev. Sci. Instrum. **88**, 043302 (2017).
[17] S. Holler, Y. Pan, R. K. Chang, J. R. Bottiger, S. C. Hill, and D. B. Hillis, Opt. Lett. **23**, 1489–1491 (1998).
[18] G. E. Fernandes, Y. L. Pan, R. K. Chang, K. Aptowicz, and R. G. Pinnick, Opt. Lett. **31**, 3034–3036 (2006).
[19] Z. Ulanowski, E. Hirst, P. H. Kaye, and R. S. Greenaway, J. Quant. Spectrosc. Radiat. Transfer **113**, 2457–2464 (2012).
[20] M. Brunel, H. Shen, S. Coetmellec, G. Gréhan, and T. Delobel, Int. J. Opt. **2014**, 143904.
[21] M. Brunel, S. Coetmellec, G. Gréhan, and H. Shen, J. Eur. Opt. Soc.: Rapid Publ. **9**, 14008 (2014).
[22] P. García Carrascal, S. González Ruiz, and J. P. A. J. Van Beeck, Exp. Fluids **55**, 1851 (2014).
[23] M. Brunel, L. Ouldarbi, H. Shen, G. Gréhan, and S. Coëtmellec, Particuology **22**, 52–58 (2015).
[24] M. Brunel, S. González Ruiz, J. Jacquot, and J. van Beeck, Opt. Commun. **338**, 193–198 (2015).
[25] L. Ouldarbi, M. Talbi, S. Coëtmellec, D. Lebrun, G. Gréhan, G. Perret, and M. Brunel, Appl. Opt. **55**, 9154–9159 (2016).
[26] M. Talbi, G. Gréhan, and M. Brunel, Appl. Opt. **57**, 6188–6197 (2018).
[27] J. Jacquot-Kielar, P. Lemaitre, C. Gobin, Y. Wu, E. Porcheron, S. Coetmellec, G. Gréhan, and M. Brunel, Opt. Commun. **372**, 185–195 (2016).
[28] M. Brunel, P. Lemaitre, E. Porcheron, S. Coëtmellec, G. Gréhan, and J. Jacquot-Kielar, Appl. Opt. **55**, 4902–4909 (2016).
[29] M. Fromager, K. Aït Ameur, and M. Brunel, Appl. Opt. **56**, 3594–3598 (2017).

[30]M. Brunel, G. Demange, M. Fromager, M. Talbi, H. Zapolsky, R. Patte, K. Aït Ameur, J. Jacquot-Kielar, S. Coetmellec, G. Gréhan, and B. Quevreux, Rev. Sci. Instrum. **88**, 083108 (2017).
[31]S. Gonzalez Ruiz and J. van Beeck, Exp. Fluids **58**, 100 (2017).
[32]B. Barkey, M. Bailey, F. N. Liou, and J. Hallet, Appl. Opt. **41**, 5792–5796 (2012).
[33]J. R. Fienup, T. R. Crimmins, and W. Holsztynski, J. Opt. Soc. Am. **72**, 610 (1982).
[34]J. R. Fienup, Opt. Lett. **3**, 27–29 (1978).
[35]J. R. Fienup, Appl. Opt. **52**, 45–56 (2013).
[36]H. Shen, L. Wu, Y. Li, and W. Wang, Appl. Opt. **57**, 4968–4976 (2018).
[37]W. Sun, T. Nousiainen, K. Muinonen, Q. Fu, N. G. Loeb, and G. Videen, J. Quant. Spectrosc. Radiat. Transfer **79-80**, 1083–1090 (2003).
[38]S. P. Groth, A. J. Baran, T. Betcke, S. Havemann, and W. Smigaj, J. Quant. Spectrosc. Radiat. Transfer **167**, 40–52 (2015).
[39]P. Yang and K. N. Liou, J. Opt. Soc. Am. A **14**, 2278–2289 (1997).